REPORT DOCUMENTATION PAGE

Public reporting burden for this collection of information is estimated to average 1 hour per response, including the time for reviewing instructions, searching existing data sources, gathering and maintaining the data needed, and completing and reviewing this collection of information. Send comments regarding this burden estimate or any other aspect of this collection of information, including suggestions for reducing this burden to Department of Defense, Washington Headquarters Services, Directorate for Information Operations and Reports (0704-0188), 1215 Jefferson Davis Highway, Suite 1204, Arlington, VA 22202-4302. Respondents should be aware that notwithstanding any other provision of law, no person shall be subject to any penalty for failing to comply with a collection of information if it does not display a currently valid OMB control number. **PLEASE DO NOT RETURN YOUR FORM TO THE ABOVE ADDRESS.**

1. REPORT DATE (DD-MM-YYYY) 05-12-2005	2. REPORT TYPE REPRINT	3. DATES COVERED (From - To)

4. TITLE AND SUBTITLE
HYPERTHERMAL REACTIONS OF $O^+(^4S_{3/2})$ WITH CD_4 AND CH_4 : THEORY AND EXPERIMENT

5a. CONTRACT NUMBER

5b. GRANT NUMBER

5c. PROGRAM ELEMENT NUMBER
61102F

6. AUTHOR(S)
D. J. Levandier*, Y-H Chiu, R.A. Dressler, L. Sun** and G.C. Schatz**

5d. PROJECT NUMBER
2303

5e. TASK NUMBER
RS

5f. WORK UNIT NUMBER
A1

7. PERFORMING ORGANIZATION NAME(S) AND ADDRESS(ES)
Air Force Research Laboratory/VSBXT
29 Randolph Road
Hanscom AFB MA 01731-3010

8. PERFORMING ORGANIZATION REPORT NUMBER
AFRL-VS-HA-TR-2005-1172

9. SPONSORING / MONITORING AGENCY NAME(S) AND ADDRESS(ES)

10. SPONSOR/MONITOR'S ACRONYM(S)

11. SPONSOR/MONITOR'S REPORT NUMBER(S)

12. DISTRIBUTION / AVAILABILITY STATEMENT
Approved for Public Release; Distribution Unlimited

*Boston College, Institute for Sci Res., Newton, MA; **Dept Chemistry, Northwestern Univ, Evanston, IL

13. SUPPLEMENTARY NOTES

14. ABSTRACT
Theoretical and experimental methods are applied to the study of the reaction dynamics in hyperthermal collisions of O^+ ($^4S_{3/2}$) with methane. Measurements of the absolute reaction cross sections for the interaction of O^+ with CD_4 and CH_4 were obtained at collision energies in the range from near-thermal to approximately 15 eV, using the guided-ion beam (GIB) technique. Product recoil velocity distributions, using the GIB time-of-flight (TOF) methods, were determined for several product ions at selected collision energies. The main reaction channel, charge transfer, proceeds via large impact parameter collisions. A number of minor channels, involving more intimate collisions, were also detected. Ab initio electronic structure calculations have been performed with different levels of theory and basis sets, including high-level coupled-cluster calculations to determine the energies of reaction intermediates and transition states for reaction. Several reaction paths on both quartet and doublet electronic states of $(O \cdot CH_4)^+$ are found, and these provide a reasonable qualitative interpretation of the experiments. Although most of the products can be produced via spin-allowed pathways, the appearance of CH_3^+ at low energies suggests that intersystem crossing plays some role.

15. SUBJECT TERMS
Ion-molecule reactions   Alkanes   Ionospheric ions   Materials degradation
Guided-ion beams   Charge transfer   Dissociative charge transfer   Recoil velocity

16. SECURITY CLASSIFICATION OF:			17. LIMITATION OF ABSTRACT	18. NUMBER OF PAGES	19a. NAME OF RESPONSIBLE PERSON R. Dressler
a. REPORT UNCLAS	b. ABSTRACT UNCLAS	c. THIS PAGE UNCLAS	SAR		19b. TELEPHONE NUMBER (include area code) 781-377-2332

Hyperthermal Reactions of $O^+(^4S_{3/2})$ with CD_4 and CH_4: Theory and Experiment

Dale J. Levandier, Yu-Hui Chiu, and Rainer A. Dressler

Space Vehicles Directorate, Air Force Research Laboratory,
Hanscom Air Force Base, Massachusetts 01731

Lipeng Sun and George C. Schatz

Department of Chemistry, Northwestern University,
Evanston, Illinois 60208-3113

Hyperthermal Reactions of $O^+(^4S_{3/2})$ with CD_4 and CH_4: Theory and Experiment[†]

Dale J. Levandier,[§] Yu-Hui Chiu, and Rainer A. Dressler*

Space Vehicles Directorate, Air Force Research Laboratory, Hanscom Air Force Base, Massachusetts 01731

Lipeng Sun and George C. Schatz*

Department of Chemistry, Northwestern University, Evanston, Illinois 60208-3113
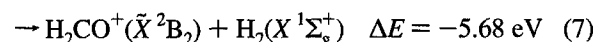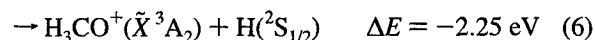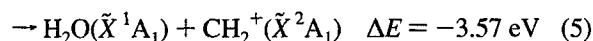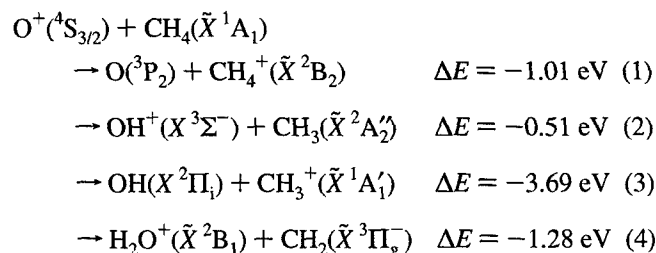
Received: May 10, 2004; In Final Form: June 4, 2004

Theoretical and experimental methods are applied to the study of the reaction dynamics in hyperthermal collisions of O^+ $(^4S_{3/2})$ with methane. Measurements of the absolute reaction cross sections for the interaction of O^+ with CD_4 and CH_4 were obtained at collision energies in the range from near-thermal to approximately 15 eV, using the guided-ion beam (GIB) technique. Product recoil velocity distributions, using the GIB time-of-flight (TOF) methods, were determined for several product ions at selected collision energies. The main reaction channel, charge transfer, proceeds via large impact parameter collisions. A number of minor channels, involving more intimate collisions, were also detected. Ab initio electronic structure calculations have been performed with different levels of theory and basis sets, including high-level coupled-cluster calculations to determine the energies of reaction intermediates and transition states for reaction. Several reaction paths on both quartet and doublet electronic states of $(O \cdot CH_4)^+$ are found, and these provide a reasonable qualitative interpretation of the experiments. Although most of the products can be produced via spin-allowed pathways, the appearance of CH_3^+ at low energies suggests that intersystem crossing plays some role.

I. Introduction

Hyperthermal reactions of cations with methane have been the subject of a number of studies, relating to such diverse areas as reactions in interstellar clouds,[1] planetary atmospheres,[2] diamond film deposition,[3−5] catalysis,[6−14] combustion,[15−18] as well as fundamental interest in reaction dynamics.[19,20] Our interest in the reactions of methane with O^+ derives largely from the effort to understand the effects of exposure of spacecraft to the low earth orbit (LEO) environment, in which this ion is the most abundant. In particular, the gas-phase O^+ + methane reactions are intended as a benchmark for developing the theory needed for understanding the origin of polymer erosion at LEO conditions. An overview of the phenomena observed in ion−organic surface interactions was given by Cooks et al.[21] The experimental work presented here is an extension of a recent study of reactions of O^+ with ethane, propane, and *n*-butane.[22]

For reactions of O^+ with methane, a large number of product channels are energetically possible, as indicated by the following incomplete list in which only ground-state species are included:[23]

$$O^+(^4S_{3/2}) + CH_4(\tilde{X}\,^1A_1)$$

$$\rightarrow O(^3P_2) + CH_4^+(\tilde{X}\,^2B_2) \qquad \Delta E = -1.01 \text{ eV} \quad (1)$$

$$\rightarrow OH^+(X\,^3\Sigma^-) + CH_3(\tilde{X}\,^2A_2'') \qquad \Delta E = -0.51 \text{ eV} \quad (2)$$

$$\rightarrow OH(X\,^2\Pi_i) + CH_3^+(\tilde{X}\,^1A_1') \qquad \Delta E = -3.69 \text{ eV} \quad (3)$$

$$\rightarrow H_2O^+(\tilde{X}\,^2B_1) + CH_2(\tilde{X}\,^3\Pi_g^-) \qquad \Delta E = -1.28 \text{ eV} \quad (4)$$

$$\rightarrow H_2O(\tilde{X}\,^1A_1) + CH_2^+(\tilde{X}\,^2A_1) \qquad \Delta E = -3.57 \text{ eV} \quad (5)$$

$$\rightarrow H_3CO^+(\tilde{X}\,^3A_2) + H(^2S_{1/2}) \qquad \Delta E = -2.25 \text{ eV} \quad (6)$$

$$\rightarrow H_2CO^+(\tilde{X}\,^2B_2) + H_2(X\,^1\Sigma_g^+) \qquad \Delta E = -5.68 \text{ eV} \quad (7)$$

In selected ion-flow tube experiments, at 298 K, the O^+ + methane system was observed to react very efficiently, at ~80% of the capture rate; however, the only products observed were those resulting from charge transfer (reaction 1) and hydride abstraction (reaction 3), in a ratio of ~5.5:1.[24,25] The very exothermic channels resulting in C−O bond formation (insertion), for example, were not observed. Interestingly, the observation of the OH + CH_3^+ hydride abstraction product channel indicates a relatively efficient crossing seam from the entrance quartet surface to the exit doublet potential surface, which is also required for reactions 5 and 7, above.

In this joint theory and experiment paper, we present the detailed results of a guided-ion beam (GIB) study of $O^+(^4S_{3/2})$ reactions with methane, in which we have measured absolute reaction cross sections at near-thermal to hyperthermal collision energies and recoil velocity distributions of several product ions at selected collision energies. The experiments were carried out using normal and perdeutero-methane, because of the many possible coincident masses among the ions of interest, most notably the reactant ion, O^+, and the normal methane charge-transfer product, CH_4^+.

Given the multitude of observed product channels, we attempt to elucidate the dynamics with ab initio calculations of the $(O \cdot CH_4)^+$ hypersurface. To the best of our knowledge, there have been no detailed theoretical studies of the potential energy surface (PES) for the $O^+(^4S)$ + CH_4 reaction system. Lyubimova and co-workers[26] calculated the relative energies of the reactants and possible products at low levels of theory and with small

Hyperthermal Reactions of O$^+$ with CD$_4$ and CH$_4$

J. Phys. Chem. A, Vol. 108, No. 45, 2004 **9795**

basis sets; however, the reaction intermediates, stationary points, and the intrinsic reaction coordinates (IRC) are still unknown. We have therefore performed high-level ab initio electronic structure calculations on the ground quartet and doublet potential energy surfaces for the O$^+$ + CH$_4$ system.

II. Methods

II.A. Experiment. The guided-ion beam instrument used in this work has been discussed in detail previously,[27] so only a brief description is given here. The system is a tandem mass spectrometer with an rf octopole ion guide located between the two mass filters. The ion guide has two stages, the first octopole of length 7.4 cm and the second of length 16.7 cm. A 3.5 cm long collision cell surrounds the ion guide and is located so that its exit is at the junction of the octopole stages. Ions pass from the first mass filter into the first octopole stage and from the second octopole stage to the second mass filter via injection and extraction lens systems, respectively.

The O$^+$ reactant, or primary, ions are formed by dissociative ionization resulting from electron impact on CO$_2$. By maintaining the electron energy at ~20 eV, which is 2.3 eV below the appearance potential for O$^+$(^{2}D), the primary ion beam is produced almost exclusively ($\geq$99%) in the ground-state O$^+$(^{4}S).[28,29] Primary ions are mass-selected in the first mass spectrometer and are then injected into the first octopole at the desired kinetic energy. Unreacted primary ions and ions produced in reactions with the target gas in the collision cell pass into the second octopole, which is typically biased 0.4–0.5 V below the first octopole to aid in the extraction of thermal product ions from the cell. At the exit of the second octopole, primary and secondary ions are injected into a quadrupole mass filter for mass analysis. The ion beam energy is known to better than ±0.1 eV, with beam spreads typically of ~0.3 eV fwhm, as measured by the retarding potential method and by time-of-flight.

Secondary reactions in the collision cell, owing to the large cross sections for reactions of the main reaction product ions, CH$_4^+$ and CH$_3^+$, with methane,[30,31] are minimized by maintaining target gas pressures in the range of 0.08–0.10 mTorr, and by periodically turning off the rf potential to allow trapped low-energy ions to escape the octopole volume.[29] In addition, the acceleration of thermal ions into the second octopole, operated at a lower bias potential than the first, further reduces secondary reactions with background gas.

As described previously,[27] absolute cross sections are determined by integrating the mass spectrometer signal intensities for the product and transmitted primary ions, monitoring the pressure of the target gas, and using the low-density limit of the Lambert–Beer expression. A background correction, due to reactions of the ion beam with the residual vacuum chamber pressure of target gas, within the whole octopole volume, is measured and applied to the data. Where a secondary product, which may be discerned in cell pressure dependence studies, is uniquely the result of the reaction of a particular primary reaction product, the cross section for the latter channel may simply be derived from the sum of the signals for primary and secondary products. Errors in the absolute cross sections, based in part on periodic calibration of the apparatus using the accepted standard reaction, Ar$^+$ + D$_2$ → ArD$^+$ + D,[27,32] are estimated to be of the order of ±30%.

Product ion time-of-flight (TOF) spectra are measured by pulsing the primary ion beam, using a 3–5 μs ion beam pulse width, and measuring the flight time of product ions arriving at the detector. A ring-shaped electrode, surrounding the octopole

at the entrance of the collision cell, is kept at ~100 V above the dc potential of the first octopole so that the small penetrating field (~0.1 V) reflects product ions that are backscattered in the laboratory frame of reference.

Perdeutero-methane (99%) was obtained from Cambridge Isotope Laboratories and normal methane (UHP) from Aimtek; the gases were used as delivered.

II.B. Computations. The ab initio electronic structure calculations reported here were performed with the GAMESS[33] and QChem[34] program packages. These calculations are based on the self-consistent-field (SCF), second-order Møller–Plesset perturbation (MP2), B3LYP hybrid density functional theory, and coupled-cluster singles-and-doubles (CCSD)[35] with perturbative triples correction (CCSD(T))[36,37] methods. The open-shell system was treated with a spin-unrestricted wave function. The basis sets used range from the 6-31G** split valence basis set to the much larger 6-311++G(3df,3pd) and aug-cc-pVTZ basis sets. Due to the flexibility of CH$_4^+$ and of the ion–molecule complexes, tight convergence criteria were employed for the structure optimization. Vibrational frequencies were calculated at all stationary points; the reported minima all have real frequencies and saddle points have only one imaginary frequency. Zero-point energy corrections were done with the unscaled frequencies from the calculations. Standard Mulliken populations were used for the analysis of charge distributions and spin densities. For most of the reactions, IRC calculations were carried out to determine the connectivity between the transition state and its corresponding reactants, intermediates, and products. The IRC calculation is relatively time consuming so this was done at the MP2/6-31G** level of theory.

III. Results

III.A. Experiment. Figures 1 and 2 show the absolute cross sections for the ionic products of reactions of O$^+$ with CD$_4$ and CH$_4$, respectively, at center-of-mass (CM) collision energies (E_T) from near-thermal to ~15 eV. The data for each cross section are binned (or interval-averaged) from over 1000 data points, the majority of which cover the energy region up to ~2.5 eV. To facilitate comparison the two plots use the same scales. In both figures, the cross section derived from the thermal rate constant for O$^+$ + CH$_4$ reactions, averaged from selected ion-flow tube (SIFT) experiments at 298 K, by Smith et al.,[24,25] is indicated. In Figure 1 the total and Langevin–Gioumousis–Stevenson[38] (LGS) capture cross sections are shown. The total cross section for the O$^+$ + CH$_4$ system, which could conceivably be investigated by O$^+$ attenuation measurements in the TOF mode (to discriminate the CH$_4^+$ product), was not determined, in part because this method cannot account for nonreactive scattering in this system, which may be important at low collision energies.

Closer inspection of Figures 1 and 2 raise several points: first, the present experimental results indicate more reaction channels than those observed in earlier thermal energy experiments; second, there are several instances where the observed product ion masses can be attributed to multiple chemical species; and, finally, the data include secondary reaction products, the masses of which may also be coincident with primary products or other secondary products. The second point provides the rationale for studying reactions of both CD$_4$ and CH$_4$ so that the shifted product ion mass coincidences due to the isotopes would permit the elucidation of the product species. In the present work, it was not possible to study ^{18}O$^+$ + CH$_4$ reactions, the products of which involve the fewest mass coincidences, since the ion source produces significant quantities of H$_2$O$^+$.
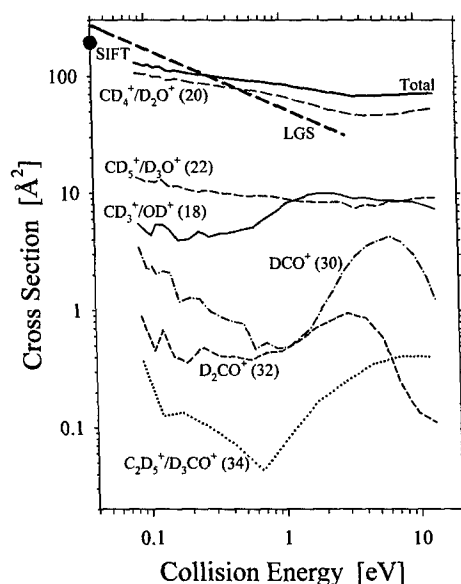
9796 *J. Phys. Chem. A, Vol. 108, No. 45, 2004*

Levandier et al.

Figure 1. Absolute cross sections for reactions of O^+ with CD_4 as a function of collision, or relative, energy (E_T). The cross sections for individual product channels are labeled with the ion species assigned to the detected product masses (indicated in parentheses, in amu). The heavy solid line is the total cross section, the heavy dashed line is the Langevin—Gioumousis—Stevenson cross section (ref 38), and the solid circle indicates the result derived from the total rate constant for the $O^+ + CH_4$ reaction measured in SIFT experiments (refs 24 and 25).

Regarding the last point above, the conditions at which the data were obtained (0.08—0.10 mTorr target gas pressure) represent a compromise between minimizing the occurrence of secondary reactions and experimental sensitivity. This compromise allowed the detection of the minor reaction products. Table 1 contains the thermal rate constants for potential secondary reactions involving normal methane with primary product ions observed in this work.[39] In practice, only the very efficient reactions of the more prominent products should produce measurable quantities of secondary products. Due to the mass coincidences, the difficulty in measuring the CH_3^+ cross section at low collision energies, as discussed below, and the fact that some of the secondary reactions lead to the same products (notably for OH^+ and H_2O^+), we have not added the cross sections for secondary reactions to those of the corresponding primary products.

The individual cross sections in Figures 1 and 2 are labeled with the one or two chemical species attributable to the respective ion masses shown. These assignments result primarily from comparison of the data in Figures 1 and 2, vis-à-vis the isotope masses. For example, the 18 amu product ions of the normal methane reactions, in Figure 2, may be uniquely assigned to H_2O^+. If it is assumed that the perdeutero-methane reactions yield all the analogous product ions, with similar branching ratios, then the 20 amu product, in Figure 1, may be ascribed predominantly to the charge-transfer product, CD_4^+, with a smaller but significant contribution of D_2O^+ at lower collision energies. In addition, reactant gas pressure dependence measurements allow several products, which might otherwise have been subject to mass coincidences, to be unequivocally assigned. In particular, the 30 and 32 amu products of perdeutero-methane reactions, in Figure 1, could in this way be assigned to DCO^+ and D_2CO^+, respectively, with negligible contributions from the possible secondary products, $C_2D_3^+$ and $C_2D_4^+$, respectively. Table 2 outlines the basis for all the product ion assignments indicated in Figures 1 and 2.

The total $O^+ + CD_4$ cross section, the extrapolation of which agrees with the SIFT results on $O^+ + CH_4$ to within the
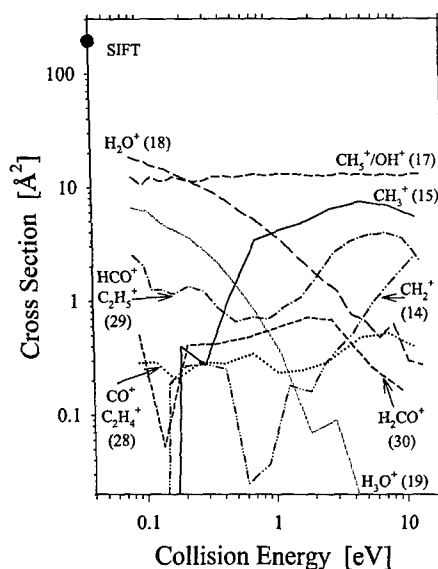

Figure 2. Absolute cross sections for reactions of O^+ with CH_4 as a function of collision, or relative, energy (E_T). The cross sections for individual product channels are labeled with the ion species assigned to the detected product masses (indicated in parentheses, in amu). The solid circle indicates the result derived from the total rate constant for this reaction measured in SIFT experiments (refs 24 and 25).

TABLE 1: Rate Constants for Possible Secondary Reactions[a]

reactant ion	rate constant $10^{-9} cm^3 s^{-1}$	main product ion (minor products)
CH_2^+	1.33	$C_2H_4^+$ ($C_2H_5^+$, $C_2H_3^+$, $C_2H_2^+$)
CH_3^+	1.04	$C_2H_5^+$
CH_4^+	1.14	CH_5^+
OH^+	1.37	H_3O^+ (CH_5^+, CH_4^+)
H_2O^+	1.14	H_3O^+ (CH_4^+)
HCO^+	<0.1	CH_5^+
H_2CO^+	0.11	H_3CO^+

[a] The indicated reactant ions are products of the $O^+ + CH_4$ reaction which were detected in the present work. The rate constants were taken from ref 39 (see references therein) for reactions of methane with the ions indicated, at temperatures in the range of 296—300 K. In each case, the main product indicated comprises, on average, at least 70% of the product ions.

combined limits of experimental error, has the form typically observed for efficient, exothermic ion—molecule reactions. That is, at low collision energy the cross section decreases, then becomes nearly constant, in this case at energies above ~3 eV. At $E_T = 10$ eV, the cross section is 71 Å^2. The LGS cross section is somewhat larger than the total cross section at the lowest energies where capture dynamics apply, that is, where the reaction should be mediated by a collision complex in which all energetically allowed reaction pathways may be sampled.

Of the CD_4 cross sections in Figure 1, the largest corresponds predominantly to the charge-transfer product, CD_4^+. The charge-transfer cross section, with the addition of the large CD_5^+/D_3O^+ secondary product cross section, constitutes as much as 80—90% of the total cross section in the energy range studied and confirms the prominence of the charge-transfer channel observed in the SIFT experiments[24,25] on normal methane. The energy dependence of the charge-transfer cross section, decreasing with energy at low collision energy and leveling off at higher energy, is typical of exothermic charge-transfer reactions, a conclusion which is not affected by the relatively small D_2O^+ contribution to the measurement. In Figure 1 the remaining cross sections for CD_3^+/OD^+, DCO^+, and D_2CO^+ exhibit a similar drop in magnitude at the lowest collision energies, then a clear minimum

TABLE 2: Identification of Reaction Product Channels with Detected Product Masses for $O^+ + CD_4$ and $O^+ + CH_4$ Reactions[a]

product mass	ions assigned	basis
		$O^+ + CD_4$
16	CD_2^+	not observable due to coincidence with O^+ mass
18	CD_3^+/OD^+	at higher E_T, σ_{18}^D is ~25% larger than σ_{15}^H, which is uniquely assigned
20	CD_4^+/D_2O^+	σ_{20}^D is an order of magnitude larger than σ_{18}^H, which is uniquely assigned
22	CD_5^+/D_3O^+	σ_{22}^D is much larger than σ_{19}^H, which is uniquely assigned; both are secondary
30	DCO^+	pressure dependence indicates negligible $C_2D_3^+$; $C_2H_3^+$ not detected
32	D_2CO^+	pressure dependence indicates negligible $C_2D_4^+$; H_2CO^+ detected
34	$C_2D_5^+/D_3CO^+$	H_3CO^+ not detected; $C_2D_5^+$ produced efficiently from $CD_3^+ + CD_4$ (cf. Table 1)
		$O^+ + CH_4$
14	CH_2^+	unique; however data are not reliable at low E_T (see text)
15	CH_3^+	unique; however data are not reliable at low E_T (see text)
16	CH_4^+	not observable due to coincidence with O^+ mass
17	CH_5^+/OH^+	σ_{17}^H is considerably larger than σ_{22}^D, which may have a small D_3O^+ component
18	H_2O^+	unique
19	H_3O^+	unique (cf. Table 1; secondary product of OH^+ and H_2O^+ reactions with CH_4)
28	$CO^+/C_2H_4^+$	not conclusive
29	$HCO^+/C_2H_5^+$	DCO^+ unique; $C_2H_5^+$ produced efficiently from $CH_3^+ + CH_4$ (cf. Table 1)
30	H_2CO^+	unique

[a] Cross sections, σ, denoted by σ_M^X, where $X = H, D$, for normal and perdeutero-methane, and M = product ion mass (amu).

in the range of 0.5–1.5 eV, and then an increase in magnitude at higher collision energies. The secondary reaction products generally track the cross sections of the respective primary product precursors.

The products of normal methane reactions, in Figure 2, largely confirm the results for perdeutero-methane. The CH_3^+ and CH_2^+ data have the following caveat: due to the need to operate the quadrupole mass spectrometer with minimal mass discrimination effects, and concomitant lower mass resolution, these measurements are affected by a large low-mass tail of the ion beam signal, which cannot be correctly accounted for at the lowest collision energies. This explains the precipitous drop in the respective cross sections at collision energies below ~2 eV, as energy is decreased; however, the ability to uniquely assign these ions, particularly CH_3^+, aids in the assignment of reaction channels.

For normal methane, the cross sections for the other channels that are also seen in perdeutero-methane reactions are quite similar to their analogues, in Figure 1. This applies particularly to the HCO^+/DCO^+ and H_2CO^+/D_2CO^+ cross sections. The H_2O^+ cross section is the only minor channel observed that has a monotonically decreasing cross section, and this suggests that the D_2O^+ contribution to the CD_4^+/D_2O^+ cross section is only important at low collision energy. The CH_2^+ cross section, where observable, exhibits enhancement with collision energy. The H_3O^+ cross section results from secondary reactions of OH^+ and H_2O^+, suggesting that these primary products must be sufficiently abundant to yield measurable quantities of the secondary product. The very small $CO^+/C_2H_4^+$ signal cannot be assigned unequivocally, however, CO^+ was not observed in the perdeutero-methane reactions. The total cross section is not shown since, again, the charge-transfer cross section cannot easily be measured. It is worth noting that the mass-related isotope effect expected from the LGS model yields a ratio of total cross sections of $\sigma_{CH_4}/\sigma_{CD_4} = 1.05$, departures from which, in thermal charge-transfer reactions of noble gas ions with normal and perdeutero-methane,[40] have been attributed to relative Franck–Condon factors at the relevant energies.[41]

Figures 3, 4, and 5 show the TOF results for several products at selected collision energies, the first two figures involving perdeutero-methane reactions and the last figure normal methane. The TOF measurements are transformed to product ion laboratory velocity distributions, $f(v_p')$, for velocity components parallel to the incident ion beam. These velocity spectra are of arbitrary scale, normalized so that the maximum amplitude
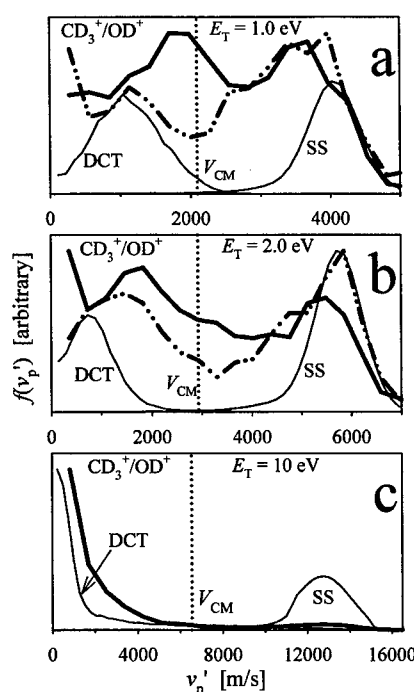

Figure 3. Laboratory velocity distributions for the CD_3^+/OD^+ (18 amu) product of $O^+ + CD_4$ reactions, transformed from ion time-of-flight measurements for collisions at (a) $E_T = 1.0$ eV, (b) $E_T = 2.0$ eV, and (c) $E_T = 10$ eV. In each plot, the heavy solid curves comprise data obtained with normal RF trapping potential (U_{RF}) and the dotted line indicates the velocity of the center of mass of the collision system (V_{CM}). The heavy "double-dot–dash" curves in (a) and (b) indicate data obtained with low U_{RF}. In each frame, the peaks indicated by thin solid lines are derived from velocity simulations, as described in the text, for backscattered CD_3^+ formed by endothermic dissociative charge transfer and OD^+ formed in a spectator stripping (ref 42) interaction, and labeled DCT and SS, respectively.

is set at 100. In each spectrum, the vertical dotted line represents the velocity of the center of mass of the colliding system, V_{CM}, which constitutes the origin of the center-of-mass (CM) reference frame. That is, taking the direction of the primary ion beam as forward in the CM frame, product ions with laboratory velocities in excess of V_{CM} exhibit recoil velocities in the forward hemisphere, while slower ions are backscattered.

In Figure 3, results are shown for the CD_3^+/OD^+ channel at (a) 1 eV, (b) 2 eV, and (c) 10 eV collision energies. At $E_T = 1$ and 2 eV the velocity distributions are essentially bimodal,
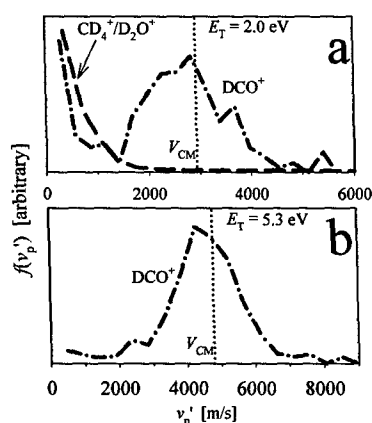
Figure 4. Laboratory velocity distributions for (a) the CD_4^+/D_2O^+ (20 amu) and DCO^+ (30 amu) products of $O^+ + CD_4$ reactions at $E_T = 2.0$ eV and (b) the DCO^+ product at $E_T = 5.3$ eV, transformed from ion time-of-flight measurements. In either plot, the dotted line indicates the velocity of the center of mass of the collision system (V_{CM}).

with substantial contributions in both the backward and forward directions. In either case, the forward and backward peaks are not symmetrically displaced with respect to V_{CM}. At $E_T = 10$ eV, the velocity distribution has evolved so that it is dominated by a large near-thermal component and a much smaller and very fast, forward-scattered contribution. Each plot also contains thin solid curves, labeled "DCT" and "SS", which are derived from simulations of backscattered CD_3^+ formed by endothermic dissociative charge transfer (DCT) and OD^+ produced by spectator stripping (SS), a model in which the kinematics and energy partitioning are well-defined.[42] The velocity simulations, which include experimental broadening effects, are derived via the osculating complex model,[43] in which direct interactions may be described as involving a very small complex lifetime relative to the complex rotational period.[44,45] For the endothermic DCT reaction, in which CD_3^+ is formed by loss of D from CD_4^+, the simulation involves the transfer of 0.75 eV of kinetic energy to internal, which corresponds to the threshold for this channel and limits the dissociation process to negligible recoil velocity, and assumes that the initial charge-transfer step involves the maximum recoil velocity. The heights of the simulated velocity distributions are arbitrary and are adjusted for ease of comparison.

Also shown in Figure 3, parts a and b, are the results of TOF measurements of the CD_3^+/OD^+ product channel, at the respective collision energies, obtained with the octopole ion guide operating at low trapping RF potentials, U_{RF}. At the lower trapping potential, ~ 20 V_{rms}, corresponding to an effective octopole trapping potential[46] of 0.7 V, product ions that have a large velocity component perpendicular to the ion beam axis are not efficiently trapped and so are not observed. At the higher, normal trapping potential, 110 V_{rms} or an effective potential of 18 V, all product ions are trapped, which is easily confirmed by monitoring product signal while varying U_{RF}. In both the low-U_{RF} velocity spectra in Figure 3, parts a and b, relative product ion intensity is lost in the region of V_{CM}, indicating substantial scattering at wide angles. This loss of product intensity appears to affect the backscattered velocity distribution more strongly than the forward-scattered component, with the net result that the minimum between these features, in both velocity spectra, shifts lower to near V_{CM}.

In Figure 4a, the low-energy data include velocity spectra for both the CD_4^+/D_2O^+ and DCO^+ channels. The former case is dominated by strong backscattering, giving a near-thermal laboratory frame distribution. In contrast, while the DCO^+
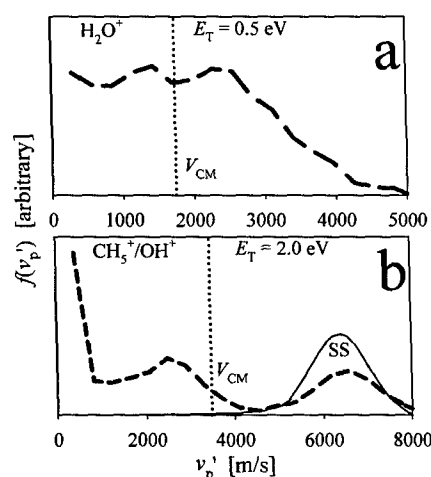

Figure 5. Laboratory velocity distributions for (a) the H_2O^+ (18 amu) product of $O^+ + CH_4$ reactions at $E_T = 0.5$ eV and (b) the CH_5^+/OH^+ products at $E_T = 2.0$ eV, transformed from ion time-of-flight measurements. In either plot, the dotted line indicates the velocity of the center of mass of the collision system (V_{CM}), and in (b) the thin solid curve labeled "SS" is derived from velocity simulations for OH^+ formed in a spectator stripping (ref 42) interaction.

distribution has a significant thermal component, there is a large contribution centered near V_{CM}. In Figure 4b, at the higher collision energy, $E_T = 5.3$ eV, the DCO^+ velocity distribution is dominated by the component centered at V_{CM}.

The TOF distributions for reactions of normal methane, in Figure 5, involve (a) the H_2O^+ channel at $E_T = 0.5$ eV and (b) the CH_5^+/OH^+ channel at $E_T = 2$ eV. In the former case, the velocity distribution is broad and appears to be centered at V_{CM}, with peaks of similar intensity in the forward and backward directions. In the CH_5^+/OH^+ spectrum, there are three obvious contributions: two backscattered components, one of which is near-thermal, and a fast, forward-scattered peak. The thin solid curve is the simulated OH^+ velocity distribution for the spectator stripping model.[42]

III.B. Computation. The intermediates and transition state structures obtained from the present MP2 calculations on the quartet and doublet electronic potential energy surfaces are shown in Figures 6 and 7, respectively, and are summarized in Table 3, along with comparisons to other methods and to values derived from experiment. Secondary dissociation and isomerization channels involving the CH_3O^+ and H_2CO^+ products of the primary reaction are shown in Figure 8, and are summarized in Table 4, where the results are compared to B3LYP calculations. The MP2 relative energies, in Tables 3 and 4, are also summarized in the reaction path diagrams in Figures 9 and 10, respectively, which also depict the results of the IRC determinations.

Numerous tests of the accuracy of the present electronic structure methods were performed. These show that spin contamination is very small (1−4% error in $<S^2>$) for all of the stationary points, justifying the use of unrestricted open-shell wave functions for all calculations. It is also found that electron correlation is important in this charged, high-spin, open-shell system; therefore, the results of UHF calculations (not shown) are not further discussed. Better performance is obtained with MP2, which gives overall good agreement with experiments or high-level (CCSD(T)) calculations, as shown in Table 3.

Previous studies[47−50] have shown that the MP2/6-31G(d,p) method gives the correct C_{2v} minimum energy structure of the CH_4^+ radical cation and the equilibrium bond lengths and angles are in reasonable agreement with high-level ab initio calcula-

TABLE 3: Relative Energies of Reactants, Intermediates, Transition States, and Products of the (O·CH$_4$)$^+$ System^a

chemical species	MP2/6-31G**	B3LYP/6-31G**	MP2/6-311++G (3df,3pd)	CCSD(T)^b	exptl^d
O$^+$ + CH$_4$	0.0	0.0	0.0	0.0	0.0
O + CH$_4$$^+$	−0.38 (−0.56)^c	−1.34 (−1.57)	−0.58 (−0.75)	−0.67 (−0.85)^d	−1.01
QCP1	−1.45 (−1.57)	−2.61 (−2.74)	−1.63 (−1.74)	−1.75 (−1.86)	
QTS2	−0.44 (−0.61)	−1.78 (−1.96)	−0.63 (−0.79)	−0.82 (−0.98)	
QCP2	−1.42 (−1.72)	−2.72 (−3.01)	−1.68 (−2.00)	−1.75 (−2.05)	
CH$_3$O$^+$ + H	−1.41 (−1.73)	−2.70 (−3.01)	−1.64 (−1.96)	−1.71 (−2.03)	−2.25
CH$_3$$^+$ + O + H	1.20 (0.82)	0.69 (0.33)	1.22 (0.85)	1.14 (0.78)	0.75
CH$_3$ + OH$^+$	0.04 (−0.19)	−0.66 (−0.89)	−0.12 (−0.33)	−0.23 (−0.44)	−0.51
QTS1	0.65 (0.38)	−1.01 (−1.29)	0.33 (0.09)	0.07 (−0.17)	
H$_2$CO$^+$ + 2H	−0.41 (−1.03)	−1.05 (−1.62)	−0.51 (−1.08)	−0.41 (−0.97)	−1.23
QTS3	−0.37 (−0.54)	−2.10 (−2.28)	−0.62 (−0.78)	−0.91 (−1.07)	
H$_2$O$^+$ + CH$_2$	−0.67 (−0.83)	−1.40 (−1.59)	−0.90 (−1.14)	−0.92 (−1.15)	−1.28
CH$_2$$^+$ + O + H$_2$	2.23 (1.72)	1.51 (1.01)	2.28 (1.78)	2.05 (1.55)	1.56
DCP1	−5.92 (−5.87)	−7.40 (−7.28)	−6.46 (−6.44)	−6.20 (−6.18)	
DTS1	−2.32 (−2.44)	−4.34 (−4.40)	−2.96 (−3.08)	−2.92 (−3.04)	
H$_2$CO$^+$ + H$_2$	−4.67 (−4.96)	−5.90 (−6.14)	−5.01 (−5.30)	−5.12 (−5.41)	−5.68
DTS2	−4.90 (−4.90)	−5.92 (−5.93)	−5.46 (−5.46)	−5.23 (−5.22)	
DCP2	−6.57 (−6.45)	−7.40 (−7.28)	−7.04 (−6.90)	−6.75 (−6.61)	
CH$_2$$^+$ + H$_2$O	−2.73 (−2.80)	−3.37 (−3.57)	−3.33 (−3.53)	−3.15 (−3.34)	−3.57
OH + CH$_3$$^+$	−2.98 (−3.12)	−3.85 (−3.99)	−3.34 (−3.47)	−3.40 (−3.53)	−3.69
DTS3	−3.23 (−3.29)	−4.47 (−4.56)	−3.85 (−3.91)	−3.51 (−3.57)	

^{a} Energies are in eV. ^{b} CCSD(T)/aug-cc-pVTZ//MP2/6-311++G(3df,3pd), ZPE corrections are based on the frequencies obtained from MP2/6-311++G(3df,3pd) calculations. ^{c} Data in parentheses are ZPE corrected. ^{d} The adiabatic IP for CH$_4$ is from ref 50 and that for the O atom is from the NIST Web site http://webbook.nist.gov/chemistry. The rest of the experimental values are derived from the heats of formation at room temperature from ref 23 and from the NIST Web site.
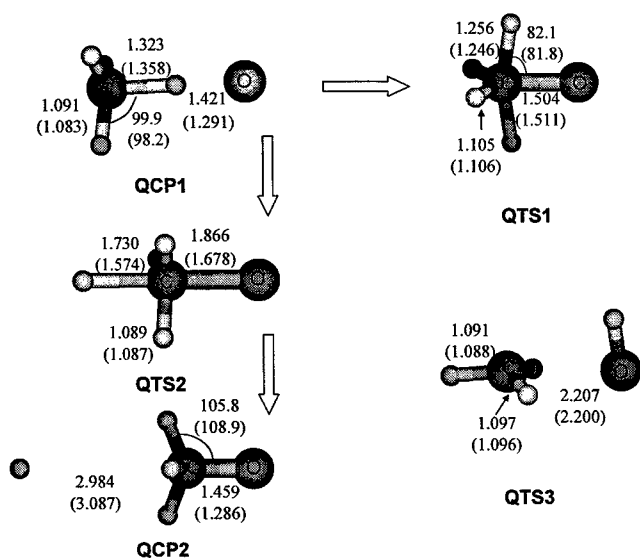

Figure 6. Optimized molecular structures of the intermediates and transition states on the quartet electronic PES. Bond distances and angles shown along with the structure are results of MP2/6-31G(d,p) results. Numbers in the parentheses are the MP2/6-311++G(3df,3pd) results. The structures are assigned names, for ease of reference in the text (Q = quartet; CP = complex; TS = transition state).

Figure 7. Optimized molecular structures on the electronic doublet (D) PES. Notations are the same as that explained in Figure 6.

tions.[47,48] Also, MP2/6-311++G(3df,3pd) calculations show very good agreement with MRCI calculations.[48] B3LYP hybrid density functional calculations for the intermediates and saddle points seem to have systematically lower energies than MP2 results but give very good product energetics. However, B3LYP density functional calculations give an equilibrium structure for CH$_4$$^+$ that has an incorrect (D_{2d}) symmetry. This failure to locate the C_{2v} structure was previously argued to be due to insufficient treatment of electronic correlation in the B3LYP density functional.[51] On the basis of this information, our subsequent discussion is based on the MP2 calculations.

Due to the fluctional nature of the methane radical cation, geometry optimization leads to different ion−dipole prereaction complexes at different levels of theory with different basis sets. Only the most stable structure (H$_3$C−H−O)$^+$ is shown in Figure
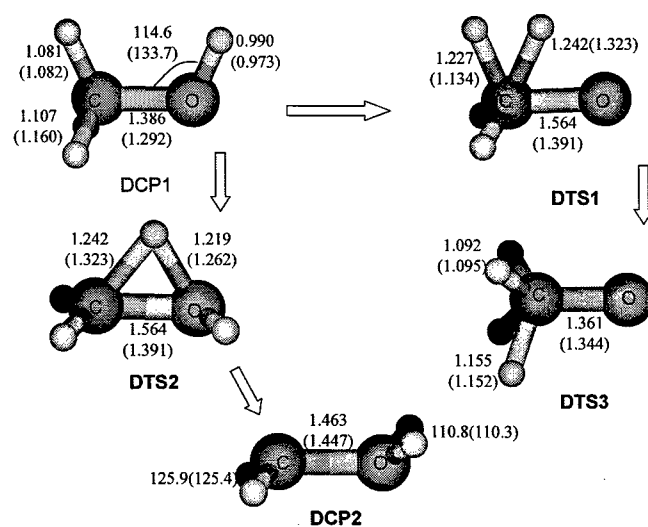
6, and we have denoted this QCP1 (the first letter Q indicates that the stationary point is on the quartet PES). It can be seen from Figure 6 that the structure of the CH$_4$ moiety in QCP1 is very close to that of the C_{3v} structure of the CH$_4$$^+$ radical cation. In addition, even though the intermolecular separation between the O and CH$_4$ moiety is about 2.65 Å, the O−H distance is rather short. With a moderate 6-31G** basis set, a charge distribution analysis shows that most of the charge is on the CH$_4$ fragment (0.68). The small bond order of H−O (0.3) indicates that only a small partial bond is formed. As expected, when using the larger 6-311++G (3df,3pd) basis set, the H−O distance is further contracted, while the C−H distance is elongated. The energy of QCP1 in our more reliable calculations is about 1.7 eV (1.9 eV with zero-point correction) below the reagent energy, so this complex should play an important role in low-energy collisions (less than 2 eV), and a lesser role at higher energies.

As shown in Figure 9, the lowest energy reaction path on the quartet PES was found to be an S$_N$2 pathway that leads
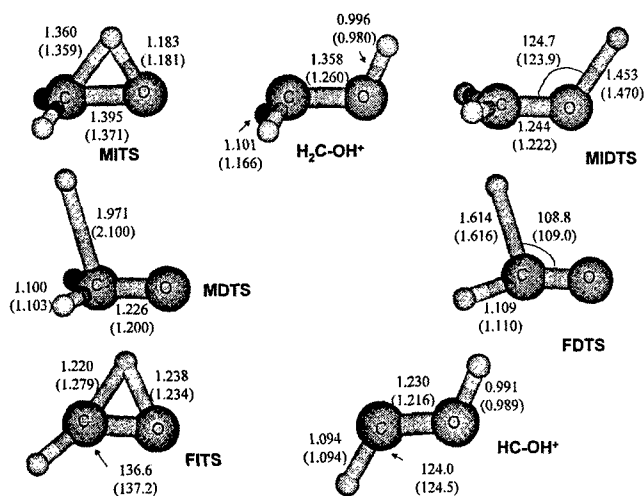
Figure 8. Optimized structures of the stationary points on the CH_3O^+ (M; methoxy ion) and H_2CO^+ (F; formaldehyde ion) isomerization (I) and dissociation (D) pathways.

TABLE 4: Energies (eV) of Stationary Points on the Dissociation Pathways of CH_3O^+ and H_2CO^+

chemical species	MP2/6-31G**	B3LYP/6-31G**	MP2/ 6-311++G (3df,3pd)
MDTS[a]	1.15 (0.96)[c]	1.29 (1.06)	1.06 (0.87)
H_2C-OH^{+a}	0.65 (0.65)	0.54 (0.54)	0.27 (0.31)
MITS[a]	1.77 (1.68)	1.85 (1.75)	1.67 (1.60)
MIDTS[a]	2.11 (1.91)	1.86 (1.66)	2.04 (1.86)
FDTS[b]	1.03 (0.87)	1.61 (1.42)	0.82 (0.63)
$HC-OH^{+b}$	−0.01 (−0.06)	0.29 (0.33)	−0.14 (−0.10)
FITS[b]	1.84 (1.72)	2.10 (1.99)	1.69 (1.59)

[a] Zero-energy reference is CH_3O^+. [b] Zero-energy reference is H_2CO^+. [c] Data in parentheses are ZPE corrected.
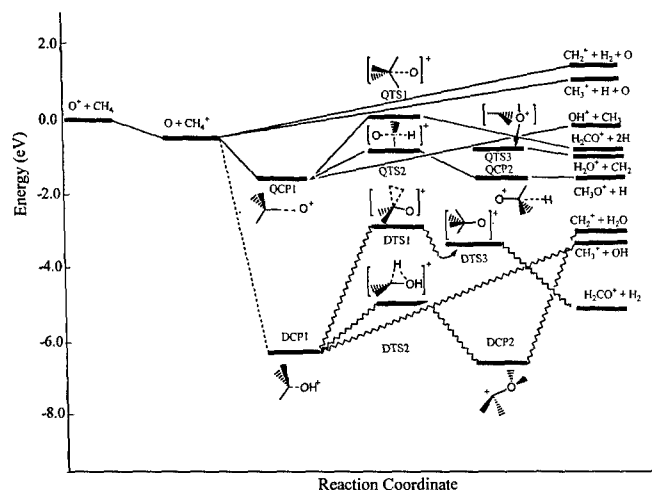

Figure 9. Diagram of the primary reaction channels. The stationary points are labeled as described in Figures 6 and 7 (Q = quartet; D = doublet; CP = complex; TS = transition state).

from QCP1 to the formation of CH_3O^+ + H. A postreaction complex (QCP2) was found on this path in which the charge is mostly on the CH_3O^+ moiety. A CCSD(T) single-point calculation shows that the QTS2 transition state between QCP1 and QCP2 is 0.15 (0.14) eV below the O + CH_4^+ asymptote and is connected to the QCP1 and QCP2 intermediates. This channel is energetically quite favorable. However, since there is a large geometry change from QCP1 to QTS2, strong coupling between the intermolecular and intramolecular modes will be required for the system to follow this reaction path. This suggests that the CH_3O^+ product may not be as favorable as one might expect and, moreover, even if CH_3O^+ is formed, subsequent processes
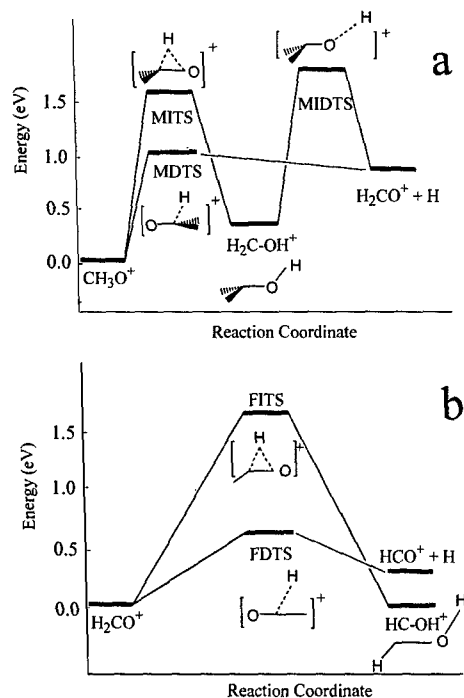

Figure 10. Diagram of the (a) CH_3O^+ (M = methoxy ion) and (b) H_2CO^+ (F = formaldehyde ion) isomerization (I) and dissociation (D) pathways.

that we describe later can lead to the dissociation of CH_3O^+ such that it is not an important product.

Two other reaction paths on the quartet surface connect QCP1 to products, either directly to OH^+ + CH_3, or via a transition state (QTS1) that is slightly (0.07 eV) above the reactants and leads to the formation of H_2CO^+ + 2H. One might expect that QCP1 connects to a reaction path in which C−H bond scission occurs to produce the CH_3 + OH^+ products. A search for a transition state for this path was not successful, suggesting that there is no potential energy barrier for the reverse CH_3 + OH^+ association reaction. The charge in QTS1 is mostly on the CH_4 moiety and a large spin density is found on the O atom. The ZPE-corrected barrier height at the CCSD(T) level is 1.69 eV with respect to the QCP1 complex. Since the H_2CO^+ product also results from dissociation of CH_3O^+, as discussed below, the potential energy surface along the IRC from QTS1 toward products exhibits a shallow well which is related to the deep potential energy well of QCP2.

A third transition state structure (QTS3) obtained on the quartet ground-state PES connects to the H_2O^+ + CH_2 products. The positive charge in QTS3 is on the OH moiety, so this structure "looks" like an ion−induced dipole structure associated with CH_3 + OH^+. However, QTS3 is a saddle point with an imaginary frequency of 358 cm^{-1}. At a low level of theory (MP2/6-31G*) we find that QTS3 connects the reaction intermediate (QCP1) with H_2O^+ + CH_2, thus providing a direct path for the production of H_2O^+ from the reactants. However, with higher level theory (see Table 3) we find that the unstable mode in QTS3 corresponds to CH_3 internal rotation about its C_{3v} axis, so we have been unable to establish its connection to QCP1 or to CH_3 + OH^+. There is, however, another mechanism for producing H_2O^+ that trajectory calculations[52] show is more efficient, namely, double abstraction in which first one, then a second H-atom is transferred to the O in a single collision. This does not seem to be associated with a single reaction path, but it competes with the OH^+ formation cross section, with no threshold for formation.

The remaining pathways on the quartet PES indicated in Figure 9 are endothermic channels producing CH$_3$$^+$ and CH$_2$$^+$ from the nascent charge-transfer product, via a collision-induced dissociation. These pathways, which may alternately be described as the endothermic DCT mechanism depicted for CH$_3$$^+$ above, are barrierless, with thresholds at 0.75 and 1.6 eV, respectively, and contrast with the chemical reactions (formation of C$-$O or O$-$H bonds) represented on the remainder of the quartet and on the doublet surfaces. Below these thresholds, the CH$_3$$^+$ and CH$_2$$^+$ ions may only be formed via spin-forbidden pathways.

Reactions on the doublet PES are all more exothermic for a given product ion than their quartet counterparts. Also the doublet transition states have energies that are lower than that of the O$^+$ + CH$_4$ reactants, so reaction on this surface should be efficient at low energy if intersystem crossing occurs. The reaction intermediate H$_3$C$-$O$-$H$^+$ (DCP1) is formed by O insertion into the CH bond of CH$_4$$^+$. The estimated well depth is -6.18 eV. DTS1 is a transition state that is 3.14 eV above the DCP1 minimum. The reaction path following from DTS1 fails when it reaches the point where the geometry is close to that of DTS3 from which the IRC proceeds to the H$_2$CO$^+$ + H$_2$ products. We infer that there must be an intermediate between DTS1 and DTS3, but it has not been found. However, this is probably not important to the reaction dynamics as there is no deep well after DTS1. The Mulliken charge on the O atom in the DTS3 structure is slightly negative (-0.25) and the C$-$O bond length is 1.344 Å, while a spin density calculation shows that the unpaired electron is on the O atom. The bond order indicates that a single bond between C and O is formed at this point. There is one imaginary frequency of 1550 cm^{-1} which corresponds to scrambling of the H-atoms.

The other doublet reaction paths, for H$_3$C$-$OH$^+$ → CH$_3$$^+$ + OH and H$_3$C$-$OH$^+$ → CH$_2$$^+$ + H$_2$O, were studied before by Radom and co-workers[53] and are in agreement with the results presented here. In addition to the latter isomerization pathway, through DTS2 and DCP2, H$_3$C$-$OH$^+$ can also dissociate to H + H$_2$C$-$OH$^+$ by CH bond fission.[53] Under hyperthermal conditions, H$_2$C$-$OH$^+$ can fragment to either CH$_2$ + OH$^+$ or CH$_2$$^+$ + OH.

In addition to the reaction and DCT mechanisms summarized in Figure 9, secondary dissociation of the CH$_3$O$^+$ and H$_2$CO$^+$ radical cations is also possible. Our ab initio calculations located two reaction pathways for CH$_3$O$^+$ dissociation to H$_2$CO$^+$ as summarized in Figure 10a. The lower energy reaction channel involves direct loss of H by passing over the 0.87 eV MDTS barrier. The second pathway involves first isomerization over the MITS barrier (1.60 eV) to form the H$_2$C$-$OH$^+$ isomer and then OH bond fission over the MIDTS barrier (1.86 eV). H$_2$CO$^+$ dissociation is a well-studied problem, and both ab initio calculations[54-56] and experimental[57] studies have been carried out to characterize the H$_2$CO$^+$ dissociation mechanisms pictured in Figure 10b. Similar to CH$_3$O$^+$, H$_2$CO$^+$ can undergo isomerization (over FITS) to give HCOH$^+$ and H-atom loss (over FDTS) to give HCO$^+$ + H. The overall reaction sequence O$^+$ + CH$_4$ → H$_2$CO$^+$ + 2H → HCO$^+$ + 3H is exothermic by 0.43 eV and is expected to occur readily. The structures involved in the CH$_3$O$^+$ and H$_2$CO$^+$ secondary dissociation processes are shown in Figure 8.

IV. Discussion

The current experiments on hyperthermal reactions of O$^+$ with methane confirm the occurrence of many of the products predicted by the electronic structure and IRC calculations, namely: CH$_2$$^+$(CD$_2$$^+$), CH$_3$$^+$ (CD$_3$$^+$), CH$_4$$^+$ (CD$_4$$^+$), OH$^+$ (OD$^+$), H$_2$O$^+$ (D$_2$O$^+$), HCO$^+$ (DCO$^+$), and H$_2$CO$^+$ (D$_2$CO$^+$). For several of these channels the present results contain evidence of the mechanisms involved. The large total cross section for the O$^+$ + CD$_4$ system, through the hyperthermal collision energy region, indicates that the system is dominated by interactions at large impact parameter. This is consistent with charge transfer, reaction 1, being the main reaction channel, and is corroborated by the CD$_4$$^+$/D$_2O^+$ TOF data, in Figure 4a. Comparison of the magnitudes of the CD$_4$$^+$/D$_2O^+$ and H$_2$O$^+$ cross sections at E_T = 2 eV, in Figures 1 and 2, respectively, suggests that the CD$_4$$^+$/D$_2O^+$ velocity spectrum involves no more than ~3% of D$_2$O$^+$; therefore, the large near-thermal velocity component in Figure 4a points to long-range, quasi-resonant charge transfer, with negligible momentum transfer between the colliding moieties.

Overall, our ab initio electronic structure calculations have found a large number of energetically accessible products that can be produced via reaction paths starting from O$^+$ + CH$_4$. Although there is only a single spin quartet electronic state (O$^+$(^{4}S$_{3/2}$) + CH$_4$) in the entrance channel, charge transfer can produce O(^{3}P) + CH$_4$$^+$($\tilde{X}$ ^{2}B$_2$) in both quartet and doublet states. Since charge-transfer reaction is 1.0 eV exothermic, a modest vibrational displacement in the CH$_4$$^+$ bending mode (E) leads to surface crossing even when the reactants are infinitely separated. Of course, charge transfer does not occur unless the two states have sufficient coupling. In detailed ab initio calculations that we will present later,[52] we find that electronic coupling between the charge-transfer channels increases abruptly at a center-of-mass separation of roughly $R = 5.0$ Å, a point where the ion$-$induced dipole interaction energy is still quite small and the quartet and doublet states are nearly degenerate. As a simple model of the charge-transfer dynamics, we might imagine that this distance defines a maximum impact parameter b_{max} for charge transfer. If we further assume that charge transfer occurs with 100% probability for collisions with impact parameters less than b_{max}, the cross section would simply be $\pi b_{max}^2 = 79$ Å^2, which agrees well with the present total cross section measurements on reactions of perdeutero-methane at higher energies (Figure 1), where the cross section is weakly dependent on energy. At lower energies, the centrifugal barrier occurs at larger R than the charge-transfer radius, which explains why capture dynamics leads here to a larger cross section than is observed. Note that all the reactive channels other than charge transfer require a relatively short-range interaction between the O and CH$_4$$^+$ to occur, so at least for high collision energies, the sum of all the reactive cross sections should not exceed roughly 22 Å^2 (the geometrical cross section for a b_{max} of 2.65 Å, the R value associated with QCP1), which is of the order of the difference between the total cross section and the sum of the charge transfer and CD$_5$$^+$/D$_3O^+$ cross sections indicated in Figure 1 (particularly at higher collision energies where the D$_2$O$^+$ has minimal contribution).

Since charge transfer occurs at a point where the two spin states are nearly degenerate, it is important to consider in what fraction of collisions spin is conserved in the charge-transfer process. However this is a difficult question to answer as, even though spin$-$orbit coupling is quite weak (<100 cm^{-1}), it is possible that the crossing region can be accessed many times once the system has become trapped in the QCP1 well. On the other hand, the large total cross section observed in the present experiments precludes domination by spin-forbidden processes. In studies of reactions of O$^+$ with acetylene, a system in which the spin-allowed (quartet) charge-transfer channel has negligible Franck$-$Condon factors for the near-resonant product state,

9802 *J. Phys. Chem. A, Vol. 108, No. 45, 2004*

Levandier et al.

compared to those for the energetically accessible spin-forbidden (doublet) charge-transfer channel, the cross section observed at collision energies below 1.5 eV was 2 orders of magnitude below the LGS capture cross section.[58,59]

The other reaction products that exhibit appreciable cross sections involve the H_2O^+ and $CH_3^+(CD_3^+/OD^+)$ channels. The former ion shows evidence of being produced in the complex-mediated interactions responsible for the velocity spectrum shown for H_2O^+ at $E_T = 0.5$ eV, in Figure 5a. The nearly symmetric velocity distribution, with respect to V_{CM}, suggests that the complex lifetime is greater than the complex rotational period at this collision energy. The form of the H_2O^+ cross section, in Figure 2, which has an $E_T^{-0.47}$ dependence at low energy, confirms this capture mechanism. This is also consistent with the barrierless pathway for H_2O^+ production via QTS3, in Figure 9, or the proposed double-abstraction mechanism.

In the case of the $CH_3^+(CD_3^+/OD^+)$ reaction channel, the situation is not as clear due largely to the fact that the CD_3^+ and OD^+ products may be scattered in both the forward or backward hemispheres, particularly at lower collision energies, as shown in Figure 3, parts a and b, where substantial scattering in both directions is observed. Further insight into the CD_3^+/OD^+ scattering may be obtained by considering the OH^+ TOF data in Figure 5b, the low-U_{RF} data in Figure 3, and the velocity simulations in both figures. In Figure 5b, the CH_5^+ contribution to the measured velocity distribution is confined to the near-thermal feature, since this ion is a product of secondary reactions. The faster peaks, therefore, indicate the production of OH^+ via two quite different collision processes, at $E_T = 2$ eV. The CM forward-scattered feature, which coincides with the spectator stripping velocity simulation, implying little translational to internal energy conversion, involves an H-atom abstraction at relatively large impact parameter. Comparison to the CD_3^+/OD^+ TOF data and to the OD^+ spectator stripping velocity simulations at $E_T = 2$ eV, in Figure 3b, suggests that the analogous D-atom abstraction may be responsible for the strongly forward-scattered feature observed in the low-U_{RF} data. Hydrogen atom abstraction reactions of methane with other ions have also been observed to occur in a stripping-like interaction.[2,60,61] The remaining TOF peak in Figure 5b indicates small impact parameter collisions, resulting in backscattered OH^+ with substantially more translational to internal energy transfer, as evidenced by the relatively small displacement from V_{CM}. The location of this feature corresponds to the region in which the substantial loss of signal is observed in the low-U_{RF} study for CD_3^+/OD^+ at $E_T = 2$ eV, in Figure 3b, and suggests that the backscattered OH^+ may involve a broad angular distribution, tailing to the forward hemisphere, as observed in Figure 5b. The same mechanisms may be expected for $OD^+(OH^+)$ production at $E_T = 1$ eV, which is supported by the coincidence of the OD^+ spectator stripping velocity simulation with the high-velocity edge of the measured distribution, and the similar loss of intensity in the low-U_{RF} data at velocities just below V_{CM}, in Figure 3a.

At $E_T = 10$ eV the scattering of CD_3^+ and OD^+ would be expected to have evolved to direct dynamics, so the two features observed in Figure 3c should comprise scattering of unique species. The location of the forward-scattered peak in Figure 3c coincides with the OD^+ simulated spectator stripping velocity distribution, as is consistent with forward-scattered OD^+ (OH^+) at lower energies. This direct pathway is supported by the calculations summarized in Figure 9.

The CH_3^+ cross section at this collision energy, in Figure 2, is of the order of 80% of the CD_3^+/OD^+ cross section, in Figure 1, and suggests that the CD_3^+ ion is responsible for the dominant, strongly backscattered feature in Figure 3c, which comprises 89% of the observed TOF signal. The large CH_3^+-(CD_3^+) cross section is consistent with a mechanism that involves a relatively large impact parameter, a picture that points to DCT, or possibly hydride abstraction (reaction 3), either of which may yield strongly backscattered product. The results in Figure 9 confirm that the $CH_3^+(CD_3^+)$ product observed at low energy in the present study, and in the earlier thermal experiments,[24,25] can arise only on the doublet PES, and are consistent with the spin-forbidden hydride abstraction mechanism. Evidence that hydride abstraction may proceed via a stripping mechanism, resulting in strongly backscattered ion product, has been observed in reactions of ions with ethane.[62,63]

Two observations, however, argue against a predominance of a spin-forbidden mechanism at higher collision energies: the magnitude of the cross section, particularly at energies above 1 eV and the rise in cross section above $\sim$0.5 eV. These observations are more consistent with DCT or a nonadiabatic CID mechanism, which has a 0.75 eV threshold. Taking thermal broadening into account, the rise in cross section with energy is consistent with the DCT thermochemical onset. The DCT simulations shown in Figure 3 are fully consistent with the observed backscattered bands. The high-velocity edge of the CD_3^+ DCT peak simulation for $E_T = 10$ eV occurs at lower laboratory velocity than the edge of the observed near-thermal component, in Figure 3c. This may signify that, if endothermic DCT contributes significantly to this channel, the interaction involves substantially more kinetic energy transfer than is required to surmount the threshold. At $E_T = 1$ eV, which is just above the DCT threshold, the CD_3^+ velocity simulation for threshold excitation lies very near, but slightly below, the low-U_{RF} backscattered peak, in Figure 3a, implying slightly above-threshold excitation. Above-threshold excitation is more obvious at $E_T = 2$ eV, where the CD_3^+ DCT velocity simulation peaks at substantially lower laboratory velocities than the backscattered feature in the low-U_{RF} data, in Figure 3b. However, the low-velocity edges of simulation and experiment agree nicely. The endothermic DCT may also occur in collisions at smaller impact parameters, resulting in a rebounding CD_3^+ fragment that is forward scattered. Velocity simulations (not shown in Figure 3) for this process were also conducted, and indicate that some of the CD_3^+/OD^+ forward scattering intensity at velocities below the OD^+ spectator stripping feature may be due to this mechanism, particularly at the lower collision energies. Similarly, DCT may also account for the CH_2^+ cross section at higher collision energies, however, the role of the exothermic, reactive doublet pathway at lower energies cannot be ascertained from the present experimental results.

The TOF results are consistent with the DCT mechanism, however, they do not preclude a complex-mediated pathway, comprising the dissociation of DCP1, or another spin-forbidden mechanism that involves initial reaction on the quartet surface to produce $CH_3 + OH^+$, followed by charge transfer to produce $CH_3^+ + OH$ while the products are separating. As long as the reaction intermediate is sufficiently vibrationally excited, the crossing between doublet and quartet surfaces should be easily accessed, providing many opportunities for intersystem crossing during the collisions. The first of these alternate mechanisms may play a role at low collision energies, and the second mechanism may be relevant at higher collision energies.

Another possible mechanism for CD_3^+ formation is via dissociation of CD_3O^+, an endothermic pathway with the same 0.75 eV thermodynamic threshold. Dissociation of CH_3O^+ on

Hyperthermal Reactions of O^+ with CD_4 and CH_4

J. Phys. Chem. A, Vol. 108, No. 45, 2004 **9803**

the quartet surface, although not shown in the reaction pathway diagram in Figure 9, does connect to the endothermic CH_3^+ + O + H products. For CD_3^+ formed by this mechanism, simulated velocity distributions were calculated (not shown in Figure 3) in which kinetic energy transfer was limited to the energetic threshold. The resulting CD_3^+ velocity distributions, both forward and backward, were located very near V_{CM}, largely because the initial exothermic process results in the recoil velocity residing largely in the lighter D product. The experimental results therefore do not preclude this mechanism, but the low-U_{RF} data, in Figure 3, parts a and b, limit the role of this mechanism to the relatively small signal observed at low CM velocity at these trapping conditions.

Formation of the $HCO^+(DCO^+)$ insertion product is exothermic by 4.6 eV and, as indicated in Figure 10b, results from fragmentation of $H_2CO^+(D_2CO^+$; reaction 7) via FDTS. The similar form of the DCO^+ and D_2CO^+ cross sections, uniquely assigned in Figure 1, supports this mechanism. The bimodal nature of these cross sections suggest two mechanisms, an exothermic route at low collision energy, where the DCO^+ cross section exhibits $E_T^{-0.9}$ behavior, and an endothermic pathway corresponding to the sharply increasing region at higher energy. The H_2CO^+ product can be produced on both the doublet and quartet PES. On the quartet PES, this involves formation of the complex QCP1, which can then dissociate to H_2CO^+ over the QTS1 barrier. Alternatively, QCP1 can dissociate to CH_3O^+ over QTS2, and then this dissociates to H_2CO^+ + H over MDTS. Since the QTS2 and MDTS energies are both below QTS1, this second mechanism could be considered to be an important path; however, it involves the QCP1 to QCP2 conversion which, as discussed earlier, is geometrically unfavorable. On the doublet surface, H_2CO^+ can be formed via the DCP1 complex and the transition state DTS1. The relative weakness of the HCO^+/H_2CO^+ pathway observed at low collision energy may relate to this spin-forbidden mechanism or the difficulty expected for the QCP1—QCP2 conversion.

The TOF data in Figure 4 is consistent with the formation of DCO^+ via loss of light particles from the collision moiety. At $E_T = 2$ eV, in Figure 4a, the DCO^+ velocity distribution is dominated by a peak centered near V_{CM}, as is typical of complex-mediated reactions. The maximum of this feature is at V_{CM}, and the peak is relatively narrow, indicating that the velocity of the product ion is small, in the CM frame, the larger part of the recoil velocity having been carried off by the departing D and D_2 fragments. In fact, barring a mechanism in which reaction occurs directly and only at a very restricted range of impact parameters, and which involves considerable conversion of available energy to product recoil energy, the CM velocity for this heavy ion is bound to be relatively small. This explains why the DCO^+ velocity distribution is also centered near V_{CM} for $E_T = 5.3$ eV, at which energy the complex-mediated reactions seen at lower collision energy should have evolved to more direct scattering, as may also be expected for the endothermic mechanism for which this collision energy represents the maximum efficiency. It also follows that the near-thermal feature in the DCO^+ velocity distribution in Figure 4a cannot be attributed to this species and may signify a non-negligible contribution by $C_2D_3^+$ (formed by dissociation of the $C_2D_5^+$ secondary product) or, more likely, poor background correction at the very low signal levels for this product at $E_T = 2$ eV, which would affect more strongly the slow ions (in the laboratory frame).

The cross section for CH_3O^+ formation is very small in the experiments, which suggests substantial conversion of this

species to H_2CO^+ and to HCO^+, as outlined in Figure 10, or possibly dissociation to yield CH_3^+, as mentioned above. The occurrence of the remaining, very weak product, CO^+, may also be explained by dissociation of H_2CO^+, which has been studied by Lorquet et al.[56] and is not further discussed here. It was shown that this channel can be described by intersystem crossings between the first electronic excited-state ($\tilde{A}$ $^2B_2$, 3.2 eV above the ground-state PES) and the ground-state PES.

V. Conclusions

We have applied the guided-ion beam technique and accurate ab initio electronic structure calculations to investigation of reactions of $O^+(^4S_{3/2})$ with $CH_4(\tilde{X}$ $^1A_1)$ in the hyperthermal collision energy regime. The experimental methods, also applied to reactions of perdeutero-methane, were used to measure absolute reaction cross sections for each of the product ions detected, as a function of collision energy in the range from near-thermal to approximately 15 eV. Recoil velocity distributions were determined for several product ions at selected collision energies. The analysis of the experimental results, although aided by the inclusion of the perdeutero-methane studies, was difficult due to the large number of coincident masses.

The electronic structure calculations identify stationary points on both the quartet and doublet PES corresponding to the $O(^3P)$ + $CH_4^+(\tilde{X}$ $^2B_2)$ charge-transfer exit channel and are accompanied by IRC determinations. The calculations predict product channels that involve both long-range interactions, as well as chemical channels in which C—O and O—H bonds are formed. Comparison of these predictions with the experimental results yield good qualitative agreement and suggest that spin-forbidden reactions account for some of the observations. In future work[52] we will use classical dynamics calculations to provide a more quantitative test of the theory, which must account for the overall domination of spin-allowed processes.

References and Notes

(1) Curtis, R. A.; Farrar, J. M. *J. Chem. Phys.* **1985**, *83*, 2224.
(2) Nicolas, C.; Torrents, R.; Gerlich, D. *J. Chem. Phys.* **2003**, *118*, 2723.
(3) Tosi, P.; Delvai, C.; Bassi, D.; Dmitriev, O.; Cappelletti, D.; Vecchiocattivi, F. *Chem. Phys.* **1996**, *209*, 227.
(4) Tosi, P.; Cappelletti, D.; Dmitriev, O.; Giordani, S.; Bassi, D.; Latimer, D. R.; Smith, M. A. *J. Phys. Chem.* **1995**, *99*, 15538.
(5) Tosi, P.; Bassi, D.; Brunetti, B.; Vecchiocattivi, F. *Int. J. Mass Spectrom. Ion Processes* **1995**, *149/150*, 345.
(6) Aristov, N.; Armentrout, P. B. *J. Phys. Chem.* **1987**, *91*, 6178.
(7) Schultz, R. H.; Elkind, J. L.; Armentrout, P. B. *J. Am. Chem. Soc.* **1988**, *110*, 411.
(8) Sunderlin, L. S.; Armentrout, P. B. *J. Phys. Chem.* **1988**, *92*, 1209.
(9) Sunderlin, L. S.; Armentrout, P. B. *J. Am. Chem. Soc.* **1989**, *111*, 3845.
(10) Chen, Y.-M.; Clemmer, D. E.; Armentrout, P. B. *J. Am. Chem. Soc.* **1994**, *116*, 7815.
(11) Chen, Y.-M.; Armentrout, P. B. *J. Phys. Chem.* **1995**, *99*, 10775.
(12) Haynes, C. L.; Chen, Y.-M.; Armentrout, P. B. *J. Phys. Chem.* **1995**, *99*, 9110.
(13) Schröder, D.; Schwartz, H.; Clemmer, D. E.; Chen, Y.; Armentrout, P. B.; Baranov, V. I.; Böhme, D. K. *Int. J. Mass Spectrom. Ion Processes* **1997**, *161*, 175.
(14) Chen, Y.-M.; Sievers, M. R.; Armentrout, P. B. *Int. J. Mass Spectrom. Ion Processes* **1997**, *167/168*, 195.
(15) Fisher, E. R.; Armentrout, P. B. *J. Chem. Phys.* **1991**, *94*, 1150.
(16) Fisher, E. R.; Armentrout, P. B. *J. Phys. Chem.* **1990**, *94*, 4396.

9804 *J. Phys. Chem. A, Vol. 108, No. 45, 2004*

Levandier et al.

(17) Viggiano, A. A.; Dotan, I.; Morris, R. A. *J. Am. Chem. Soc.* **2000**, *122*, 352.

(18) Dotan, I.; Viggiano, A. A. *J. Chem. Phys.* **2001**, *114*, 6112.

(19) Zabka, J.; Fárník, M.; DolejxfÖek, Z.; Polách, J.; Herman, Z. *J. Phys. Chem.* **1995**, *99*, 15595.

(20) Metayer-Zeitoun, C.; Alcaraz, C.; Anderson, S. L.; Palm, H.; Dutuit, O. *J. Phys. Chem.* **1995**, *99*, 15523.

(21) Cooks, R. G.; Ast, T.; Pradeep, T.; Wysocki, V. *Acc. Chem. Res.* **1994**, *27*, 316.

(22) Levandier, D. J.; Chiu, Y.-H.; Dressler, R. A. *J. Chem. Phys.* **2004**, *120*, 6999.

(23) Lias, S. G.; Bartmess, J. E.; Liebman, J. F.; Holmes, J. L.; Levin, R. D.; Mallard, W. G. *Gas-Phase Ion and Neutral Thermochemistry*; ACS/ AIP/NBS: New York, 1988; Vol. 17, Suppl. 1.

(24) Smith, D.; Spanel, P.; Mayhew, C. A. *Int. J. Mass Spectrom. Ion Processes* **1992**, *117*, 457.

(25) Smith, D.; Adams, N. G.; Miller, T. M. *J. Chem. Phys.* **1978**, *69*, 308.

(26) Lyubimova, G. V.; Shestakov, A. F. *Kinet. Catal.* **1994**, *35*, 208.

(27) Dressler, R. A.; Salter, R. H.; Murad, E. *J. Chem. Phys.* **1993**, *99*, 1159.

(28) Li, X.; Huang, Y. L.; Flesch, G. D.; Ng, C. Y. *J. Chem. Phys.* **1997**, *106*, 1373.

(29) Levandier, D. J.; Dressler, R. A.; Chiu, Y.-H.; Murad, E. *J. Chem. Phys.* **1999**, *111*, 3954.

(30) Ikezoe, Y.; Matsuoka, S.; Takebe, M.; Viggiano, A. *Gas-Phase Ion—Molecule Reaction Rate Constants through 1986*; Mass Spectroscopy Society of Japan: Tokyo, 1987.

(31) Lias, S. G.; Eyler, J. R.; Ausloos, P. *Int. J. Mass Spectrom. Ion Phys.* **1976**, *19*, 219.

(32) Ervin, K. M.; Armentrout, P. B. *J. Chem. Phys.* **1985**, *83*, 166.

(33) Schmidt, M. W.; Baldridge, K. K.; Boatz, J. A.; Elbert, S. T.; Gordon, M. S.; Jensen, J. H.; Koseki, S.; Matsunaga, N.; Nguyen, K. A.; Su, S. J.; Windus, T. L.; Dupuis, M.; Montgomery, J. A. *J. Comput. Chem.* **1993**, *14*, 1347.

(34) Kong, J.; White, C. A.; Krylov, A. I.; Sherrill, D.; Adamson, R. D.; Furlani, T. R.; Lee, M. S.; Lee, A. M.; Gwaltney, S. R.; Adams, T. R.; Ochsenfeld, C.; Gilbert, A. T. B.; Kedziora, G. S.; Rassolov, V. A.; Maurice, D. R.; Nair, N.; Shao, Y. H.; Besley, N. A.; Maslen, P. E.; Dombroski, J. P.; Daschel, H.; Zhang, W. M.; Korambath, P. P.; Baker, J.; Byrd, E. F. C.; Van Voorhis, T.; Oumi, M.; Hirata, S.; Hsu, C. P.; Ishikawa, N.; Florian, J.; Warshel, A.; Johnson, B. G.; Gill, P. M. W.; Head-Gordon, M.; Pople, J. A. *J. Comput. Chem.* **2000**, *21*, 1532.

(35) Purvis, G. D.; Bartlett, R. J. *J. Chem. Phys.* **1982**, *76*, 1910.

(36) Urban, M.; Noga, J.; Cole, S. J.; Bartlett, R. J. *J. Chem. Phys.* **1985**, *83*, 4041.

(37) Raghavachari, K.; Trucks, G. W.; Pople, J. A.; Headgordon, M. *Chem. Phys. Lett.* **1989**, *157*, 479.

(38) Gioumousis, G.; Stevenson, D. P. *J. Chem. Phys.* **1958**, *29*, 294.

(39) Anicich, V. G. *An Index of the Literature for Bimolecular Gas-Phase Cation—Molecule Reaction Kinetics*; JPL Publication 03-19; Jet Propulsion Laboratory: Pasedena, CA, 2003.

(40) Bowers, M. T.; Elleman, D. D. *Chem. Phys. Lett.* **1972**, *16*, 486.

(41) Brundle, C. R.; Robin, M. B.; Basch, H. *J. Chem. Phys.* **1970**, *53*, 2196.

(42) Henglein, A. Stripping Effects in Ion—Molecule Reactions. In *Ion—Molecule Reactions in the Gas Phase*; Ausloos, P. J., Ed.; American Chemical Society: Washington, DC, 1966; Vol. 58, p 63.

(43) Bullit, M. K.; Fisher, C. H.; Kinsey, J. L. *J. Chem. Phys.* **1974**, *60*, 478.

(44) Dressler, R. A.; Murad, E. Ion Chemistry in the Spacecraft Environment. In *Unimolecular and Bimolecular Reaction Dynamics*; Ng, C. Y., Baer, T., Powis, I., Eds.; Wiley & Sons: Chichester, U.K., 1994; Chapter 2.

(45) Levandier, D. J.; Chiu, Y.-H.; Dressler, R. A. *J. Chem. Phys.* **2000**, *112*, 122.

(46) Gerlich, D. Inhomogeneous RF Fields: A Versatile Tool for the Study of Processes with Slow Ions. In *State-Selected and State-to-State Ion—Molecule Reaction Dynamics Part 1. Experiment*; Ng, C. Y., Baer, M., Eds.; John Wiley & Sons: New York, 1992; Vol. LXXXII, p 1.

(47) Paddonrow, M. N.; Fox, D. J.; Pople, J. A.; Houk, K. N.; Pratt, D. W. *J. Am. Chem. Soc.* **1985**, *107*, 7696.

(48) Frey, R. F.; Davidson, E. R. *J. Chem. Phys.* **1988**, *88*, 1775.

(49) Wetmore, S. D.; Boyd, R. J.; Eriksson, L. A.; Laaksonen, A. *J. Chem. Phys.* **1999**, *110*, 12059.

(50) Signorell, R.; Merkt, F. *J. Chem. Phys.* **1999**, *110*, 2309.

(51) Irle, S.; Morokuma, K. *J. Chem. Phys.* **2001**, *114*, 6119.

(52) Sun, L.; Schatz, G. C. To be published.

(53) Bouma, W. J.; Nobes, R. H.; Radom, L. *J. Am. Chem. Soc.* **1982**, *104*, 2929.

(54) Vaz Pires, M. G. C.; Lorquet, J. C. *J. Chem. Phys.* **1978**, *69*, 3242.

(55) Lorquet, J. C.; Takeuchi, T. *J. Phys. Chem.* **1990**, *94*, 2279.

(56) Barbier, C.; Galloy, C.; Lorquet, J. C. *J. Chem. Phys.* **1984**, *81*, 2975.

(57) Liu, J. B.; Van Devener, B.; Anderson, S. L. *J. Chem. Phys.* **2002**, *116*, 5530.

(58) Fukuzawa, K.; Matsushita, T.; Morokuma, K.; Levandier, D. J.; Chiu, Y.-H.; Dressler, R. A.; Murad, E.; Midey, A.; Williams, S.; Viggiano, A. A. *J. Chem. Phys.* **2001**, *115*, 3184.

(59) Chiu, Y. H.; Dressler, R. A.; Levandier, D. J.; Williams, S.; Murad, E. *J. Chem. Phys.* **1998**, *109*, 5300.

(60) Wyatt, J. R.; Strattan, L. W.; Snyder, S. C.; Hierl, P. M. *J. Chem. Phys.* **1976**, *64*, 3757.

(61) Wyatt, J. R.; Strattan, L. W.; Snyder, S. C.; Hierl, P. M. *J. Chem. Phys.* **1974**, *60*, 3702.

(62) Curtis, R. A.; Farrar, J. M. *J. Chem. Phys.* **1989**, *90*, 862.

(63) Märk, S.; Schellhammer, C.; Niedner-Schatteburg, G.; Gerlich, D. *J. Phys. Chem.* **1995**, *99*, 15587.